Applied Physics A (2021) 127:807
https://doi.org/10.1007/s00339-021-04956-1

Applied Physics A
Materials Science & Processing

Spectral and optical properties of Ruddlesden-Popper-type $Ba_3Zr_2O_7$ phosphors doped with Eu^{3+} ion

Pooja Khajuria[1] · Rubby Mahajan[1] · Ram Prakash[1] · R. J. Choudhary[2] · D. M. Phase[2]

Received: 2 August 2021 / Accepted: 23 September 2021 / Published online: 3 October 2021

Abstract
This paper reports the spectroscopic investigation of $Ba_3Zr_2O_7$ phosphors. A series of $Ba_3Zr_2O_7$: Eu^{3+} with the different molar concentrations (0–4 mol.%) of europium (Eu^{3+}) ion is synthesized by the solution combustion method. The synthesized powders are characterized systematically using X-ray diffraction, X-ray photoelectron spectroscopy, photoluminescence spectroscopy, and ultraviolet–visible spectroscopy. X-ray diffraction results indicate that the synthesized powder has a tetragonal crystal structure. X-ray photoelectron spectroscopy is used to study the elemental composition of the synthesized phosphor. Field emission scanning electron microscopy result reveals that non-uniform morphology is formed. Photoluminescence spectroscopy result shows several emission peaks due to electronic transitions of Eu^{3+} ion, and the dominant peak is observed at 613 nm due to electric dipole transition $^5D_0 \rightarrow {}^7F_2$. CIE coordinates of Eu^{3+}-activated $Ba_3Zr_2O_7$ phosphor is found to be ($x = 0.64$, $y = 0.36$) which gives bright red emission. The optical band gap of the phosphors is obtained from the diffuse reflectance spectrum and found in the range of 4.62–4.83 eV.

Keywords Combustion synthesis · XRD · XPS · FESEM · PL · UV–vis

1 Introduction

In the last couple of years, the usage of inorganic phosphor materials has been perceived to have potential application in the area of photonic devices such as in lighting and display devices, solid-state lasers, fiber optic telecommunication [1–3]. In general, a phosphor is made up of a host and an activator. A host is of transparent microcrystalline material, and a luminescent activator is doped in the host lattice to create a luminescence center [4]. Usually, the rare-earth ions [5] and the divalent transition metal ions [6] are used as an activator that gives stable emission due to *f-f* and *d-d* electronic transitions, respectively, in the host lattice. Recently, the environment-friendly white light-emitting diodes (WLEDs) are obtained by doping the rare-earth ions in a suitable host which has a significant influence to produce luminescence features in the host lattice [7]. WLEDs are largely in usage because of their low energy consumption, long lifetime, and high efficiency [8–10]. Among the various rare-earth ions Tb^{3+} [11], Eu^{3+} [12], and Dy^{3+} [13] are widely used as the dopant activator to give blue-green, red, and yellow/blue light phosphors, respectively. The Eu^{3+} ion is the most important rare-earth dopant because of an excellent red emitter in many inorganic host lattices. The Eu^{3+} doped material gave several emission peaks having transitions $^5D_0 \rightarrow {}^7F_J$ (J = 0, 1, 2, 3, 4, 5, 6).

A variety of host materials such as aluminates [14], borates [15], phosphates [16], vanadates [17], and zirconates [18] activated with rare-earth ions are synthesized by different synthesis methods for the luminescent applications. In the zirconate family, alkaline-earth zirconate materials such as $BaZrO_3$, $SrZrO_3$, and $CaZrO_3$ belonging to the perovskite structure have fascinated many research workers because of their structural diversity and physical properties [19]. The perovskite-type compounds having general formula ABO_3 (where A = Ba, Ca, Sr, Pb, Fe; B = Zr, Hf, Ti) are called an inorganic chameleon because of their huge structure flexibility, i.e., these compounds show phase transition from the mother cubic structure to the tetragonal or orthorhombic structure [20, 21]. These perovskite oxide materials have a wide variety of potential

✉ Ram Prakash
rpgiuc@gmail.com; ramprakash@smvdu.ac.in

[1] School of Physics, Shri Mata Vaishno Devi University, Katra, Jammu and Kashmir 182320, India

[2] UGC DAE Consortium for Scientific Research, Indore 452001, India

applications in luminescent materials [22], ferroelectric materials [23], and dielectric materials [24], etc.

Among the various host materials, the lanthanide ion-activated alkaline-earth perovskite oxide materials are interesting candidates as a phosphor especially for field emission and electroluminescent displays [25]. The theoretical study shows that barium zirconate exists in three phases as $BaZrO_3$, Ba_2ZrO_4, and $Ba_3Zr_2O_7$. Among them, $Ba_3Zr_2O_7$ has the most distorted structure and the distorted structure has more impact on the electrical and optical properties of the material which results in fulfilling the demands of electro-optic applications [21, 25]. $Ba_3Zr_2O_7$belongs to the Ruddlesden-Popper (RP) type structural family which is derived from the perovskite oxide. The general formula for the RP family is $A_{n+1}B_nO_{3n+1}$ where n is the number of perovskite layers. For $n=1$ the perovskite layers are interleaved with AO layers along the crystallographic c-axis, and for $n=2$ the double perovskite layers are interleaved with AO layers [26]. These structures form the tetragonal crystal structure for $n=1$, 2, 3, and for $n=\infty$ the compounds form cubic structure [21].

In the literature, several reports are available for $BaZrO_3$-activated with various lanthanide-ions (Eu, Sm, Tb, etc.) which are synthesized via different synthesis routes. Gupta et al. have synthesized the Sm^{3+} and Eu^{3+} doped $BaZrO_3$ using a self-assisted gel-combustion route and found that the resultant phosphor can be used in future white LEDs [27]. Kunti et al. have reported the local structure and spectroscopic properties of Eu^{3+} doped $BaZrO_3$. They have synthesized the phosphor via a solid-state reaction method, and the internal quantum efficiency, lifetime, and photometric studies show that the phosphor may be a good candidate for red light-emitting device applications [27]. Marı´ et al. have synthesized ZrO_2: Tb^{3+} and $BaZrO_3$: Tb^{3+} via a solution combustion method and studied morphology and luminescent properties of the synthesized phosphors [28]. To the best of our knowledge, there is no report available for the Eu^{3+} doped $Ba_3Zr_2O_7$ that belongs to the Ruddlesden-Popper structure family for the solid-state lighting application. Therefore, in the present work, we have synthesized $Ba_3Zr_2O_7$: Eu^{3+} via a combustion method as this method is a fast process, low cost, and energy-saving. The structural, surface, luminescent, and optical properties of the synthesized samples are studied using various spectroscopic techniques such as X-ray diffraction (XRD), X-ray photoelectron spectroscopy (XPS), Field emission scanning electron microscopy (FESEM), Photoluminescence (PL), and UV–Vis spectroscopy (UV–Vis).

2 Experimental

Polycrystalline europium-activated $Ba_3Zr_2O_7$ phosphors are obtained by taking Barium nitrate ($Ba(NO_3)_2$; CDH; 99.0%), Zirconyl nitrate ($ZrO(NO_3)_2$; Loba Chemie; 99.5%), Europium oxide (Eu_2O_3; Himedia; 99.99%), and Urea ($CO(NH_2)_2$; Himedia; 99.5%) as starting reagents. The phosphors are synthesized for different doping concentrations of Eu^{3+} ions by employing the solution combustion method. In this synthesis method, metal nitrates are used as an oxidizer and urea as a fuel to trigger or activate the reaction propagation. Also, the oxidizer/ fuel ratio should be unity to complete the reaction. The flowchart for the preparation of $Ba_3Zr_2O_7$: Eu^{3+} is shown in Fig. 1. The precursors are weighed according to the balanced chemical Eq. (1) and are mixed by adding a few drops of distilled water in an agate mortar.

$$9(1-x)Ba(NO_3)_2 + 6ZrO(NO_3)_2 + 25CO(NH_2)_2 + \frac{9}{2}xEu_2O_3 \rightarrow 3Ba_{3(1-x)}Zr_2Eu_{3x}O_7 + 25CO_2 + 40N_2 + 50H_2O \quad (1)$$

The mixture is ground in a mortar with the help of a pestle to obtain a thick paste. The paste is transferred into the alumina crucible and placed in the preheated muffle furnace at 660 °C. The combustion process of metal nitrate–fuel mixture involves dehydration, decomposition, swelling, and burning of the paste [29]. The reaction completes in 3–4 min by forming a white foamy product. Thereafter, the foamy product is milled in an agate mortar to obtain a fine powder, and further, the powder is annealed at 1150 °C for 4 h to get complete crystallinity.

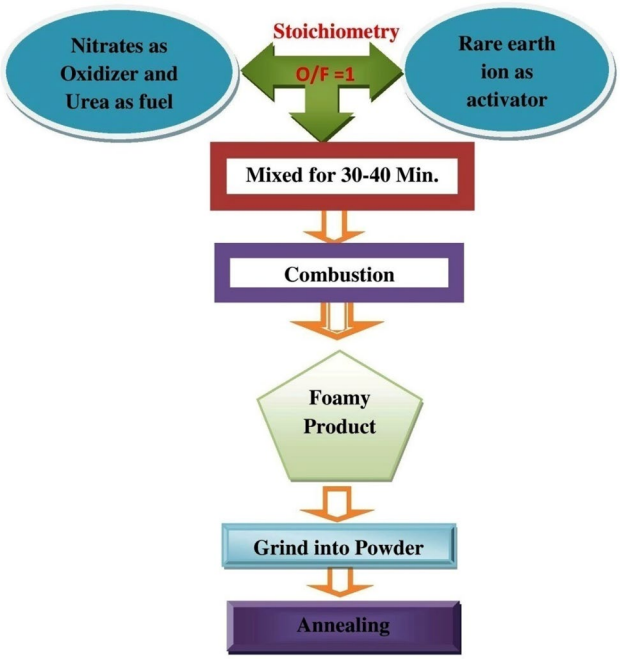

Fig. 1 Flowchart for the preparation of $Ba_3Zr_2O_7$:Eu^{3+}

2.1 Sample characterization

The crystallinity and phase identification of the synthesized sample are accomplished by XRD measurement using a standard diffractometer (Bruker D8 advance) with CuKα radiation ($\lambda = 1.5406$ Å). The X-ray photoelectron spectroscopy analysis is performed by an Omicron energy analyzer (EA-125) with AlKα (1486.6 eV) as an X-ray source to study the elemental composition of the synthesized material. FESEM analysis is carried out by Hitachi, Japan having model SU 8010 series. The photoluminescent excitation and emission spectra are measured using a Cary-Eclipse Spectrofluorometer having a xenon lamp as an excitation source with a slit width of 5 nm. The data are recorded in phosphorescence mode. The color coordinates are calculated using the Commission Internationale de I'eclairage (CIE) calculation program. The Shimadzu UV-2600 double beam spectrophotometer in the range of 190–1400 nm is used to record the diffuse reflectance spectrum of the synthesized samples.

3 Results and discussion

3.1 X-ray diffraction

The XRD pattern of $Ba_3Zr_2O_7$:Eu^{3+} phosphor along its JCPDS stick pattern is shown in Fig. 2. All the diffracted peaks of the sample are well-matched with the standard card no. 24–0131 data file having a tetragonal crystal system which belongs to space group 14/mmm (139) of $Ba_3Zr_2O_7$. In the XRD pattern, various diffraction peaks are observed at 2θ = 21.4°, 24.4°, 30.1°, 41.5°, 43.2°, 53.2°, 62.7°, 70.9°, 78.6°, and 86.0°. These peaks are indexed to (1 0 1), (1 0 3), (1 1 0), (0 0 10), (2 0 0), (2 1 5), (2 1 9), (3 0 5), (1 0 17), and (3 1 10) planes, respectively. The minimal intensity peak

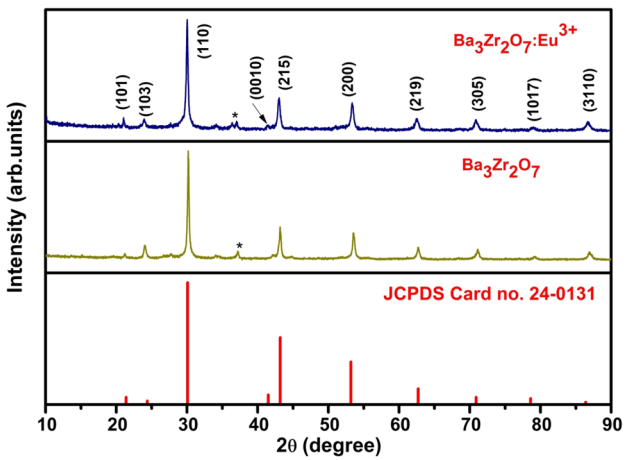

Fig. 2 XRD pattern of $Ba_3Zr_2O_7$ and $Ba_3Zr_2O_7$: Eu^{3+} (2 mol.%) along with their JCPDS cards

(marked with an asterisk) may be caused by the precursors that do not react completely during the combustion process [30]. The crystallite size of Eu^{3+}-activated $Ba_3Zr_2O_7$ and $Ba_3Zr_2O_7$ is found to be ~ 27 and ~ 38 nm, respectively which is obtained from the most intense peaks using the Debye Scherrer formula [31] given in Eq. (2)

$$D_c = \frac{K\lambda}{\beta cos\theta} \tag{2}$$

where D_c is the crystallite size of the particle, λ is the wavelength of CuKα (1.5406 Å), K is the shape factor having a value close to unity (0.9), β (in radians) is the full width at half maxima (FWHM), and θ is the Bragg angle.

The other structural parameter such as lattice parameters (a and c), and volume (V) are determined by the following relation. The lattice parameters a and c are given by Eq. (3)

$$\frac{1}{d^2} = \left(\frac{h^2 + k^2}{a^2}\right) + \frac{l^2}{c^2} \tag{3}$$

where (hkl) are miller indices and d is interplanar spacing.

The volume V of the unit cell of a tetragonal crystal structure is given by Eq. (4)

$$V = a^2 c \tag{4}$$

All the calculated values are listed in Table 1.

The calculated lattice parameter is slightly increased as compared to the standard value because of the different ionic radii of Eu^{3+} (0.1087 nm) and Ba^{2+} (0.143 nm).

4 Surface analysis

4.1 X-ray photoelectron spectroscopy

The chemical composition of the synthesized phosphor is determined by X-ray photoelectron spectroscopy. XPS survey scan of $Ba_3Zr_2O_7$: Eu^{3+} phosphor in the binding energy range of 0–1400 eV is shown in Fig. 3. The spectrum shows that the elements Ba, Zr, O, Eu, and C are present at the surface of the synthesized material. The C *1 s* peak is observed due to the carbon present in the

Table 1 The lattice parameter of $Ba_3Zr_2O_7$ and $Ba_3Zr_2O_7$: Eu^{3+} phosphor

Lattice parameter	Doped	Undoped	Standard JCPDS (24–0131)
a (Å)	4.35	4.18	4.18
c (Å)	21.7	22.5	21.72
V (Å^3)	410.61	393.12	380.99

atmosphere and is considered as a calibrating element during the XPS measurement. The XPS sharp photoelectron peaks of the elements located at 89.8, 177.0, 285.8, 529.3, 779.8–793.9, 900.1, 975.8, 1060.9, 1134.05 eV correspond to Ba *4d*, Zr *3d*, C *1 s*, O *1 s*, Ba *3d*, Ba *(MNN)*, O *(KLL)*, Ba *3p*, and Eu *3d*, respectively. The detailed scan photoemission spectra are also examined for Ba *3d*, Zr *3d*, O *1 s,* and Eu *3d* to confirm the oxidation state of the elements.

The fitted narrow scan spectra of Ba *3d*, Zr *3d*, O *1 s,* and Eu *3d* are shown in Fig. 4a. The spectrum of Ba *3d* is de-convoluted into two peaks of barium doublets $3d_{5/2}$ and $3d_{3/2}$ arising due to the spin–orbit splitting at binding energy 780.8 and 795.9 eV, respectively, consistent with 2 + state of Ba. The binding energy difference of these doublets is found to be 15.1 eV which is approximately equal to the literature value [32]. Figure 4b depicts the narrow scan spectrum of O *1 s*. The fitted peak at 530.2 eV corresponds to O *1 s* core level, and the spectrum is deconvoluted into three peaks positioned at energy 531.20, 530.07, and 528.41 eV. These peaks arise due to the bonding of oxygen with barium, zirconium, and europium, i.e., Ba–O, ZrO_2, and Eu–O [32, 33], respectively.

Figure 4c depicts the narrow scan spectrum of Zr *3d* core level. The spectrum is fitted with a single broad peak positioned at 181.9 eV corresponding to Zr $3d_{5/2}$ which exhibits a 4 + oxidation state [34]. Figure 4d depicts the narrow scan spectrum of Eu *3d* core level. The spectrum consists of a single fitted peak positioned at binding energy 1132.5 eV corresponding to Eu $3d_{5/2}$, suggesting that the Eu ions are present in the 3 + oxidation state in $Ba_3Zr_2O_7$: Eu^{3+} phosphor [35].

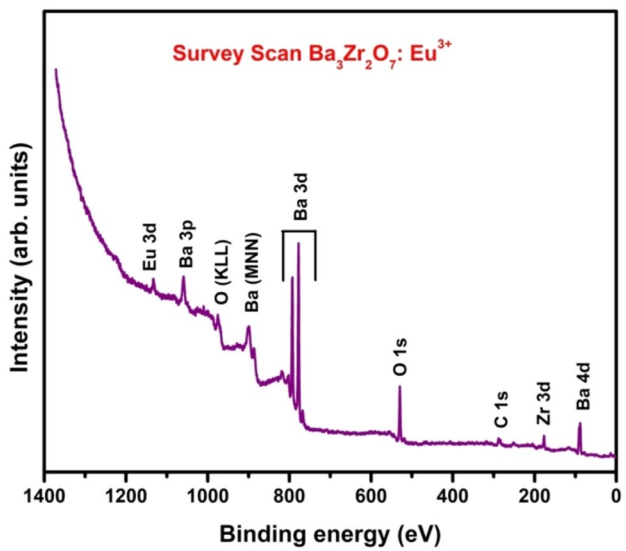

Fig. 3 XPS survey scan of $Ba_3Zr_2O_7$: Eu^{3+}

4.2 Field emission scanning electron microscopy

Figure 5 shows the FESEM image of $Ba_3Zr_2O_7$: Eu^{3+} (2 mol.%) phosphor at different magnifications. It can be seen from Fig. 5a and b, there may be a mixed (spherical + plates) morphology of the non-uniform particles with some voids, because of the emission of many gases during the synthesis process. In higher magnification, it has been observed that the particles are agglomerated with each other as the sample is annealed at a higher temperature. The average size of the particles is found from the particle size distribution histogram as shown in Fig. 5c, and the obtained value of particle size is 72 nm for $Ba_3Zr_2O_7$: Eu^{3+} (2 mol.%).

5 Luminescent studies

5.1 Photoluminescence

The PL excitation and emission spectrum of $Ba_3Zr_2O_7$:Eu^{3+} (2 mol.%) at room temperature having a wavelength range of 200–750 nm are shown in Fig. 6. The excitation spectrum is examined at 613 nm emission wavelength of Eu^{3+} ion in the range of 200–500 nm. The broad band is observed in the region 200–350 nm due to the charge transfer band (CTB) from O^{2-} *2p* filled orbital to the partially filled *4f* orbital of Eu^{3+} ion (ligands to rare-earth ions) in the host matrix ($Ba_3Zr_2O_7$), and several sharp peaks are observed in the region 360–500 nm having a prominent peak at 392 nm. These excitation bands arise because of *4f–4f* transitions of Eu^{3+} ion. The excitation peaks at 361, 380, 392, 412, and 462 nm correspond to the transition from ground state $^7F_0$ to the excited state $^5D_4$, $^5L_7$, $^5L_6$, $^5D_3$, and $^5D_2$ of Eu^{3+} ion, respectively [36].

The emission spectrum is recorded using an excitation wavelength of 257 and 392 nm in the region 500–750 nm. Several emission bands are observed in the visible region positioned at 592, 613, 652, and 704 nm are ascribed to the electronic transition from an excited state $^5D_0$ to the ground state $^7F_1$, $^7F_2$, $^7F_3$, and $^7F_4$ of Eu^{3+} ion, respectively. In all the emission peaks of $Ba_3Zr_2O_7$: Eu^{3+}, the transition $^5D_0 \rightarrow {}^7F_1$ (592 nm) is the purely magnetic dipole transition (MDT) with the selection rule $\Delta J = \pm 1$ and the transition $^5D_0 \rightarrow {}^7F_2$ (613 nm) is a purely electric dipole transition (EDT) with the selection rule $\Delta J = \pm 2$ being the most prominent peak. This prominent peak gives intense red emission. Some other weak emission peaks are also observed having transition $^5D_0 \rightarrow {}^7F_3$ (652 *nm*) and $^5D_0 \rightarrow {}^7F_4$ (704 nm) of Eu^{3+} ion [37]. In this study, the hypersensitive electric dipole transition is dominant in the emission spectrum, which indicates that the Eu^{3+} ion is located at a low symmetry site in the host lattice. Moreover, the fine splitting of emission peaks of Eu^{3+} ($^5D_0$—$^7F_{1,\,2,\,3,\,4}$) ion can be seen in the emission spectrum

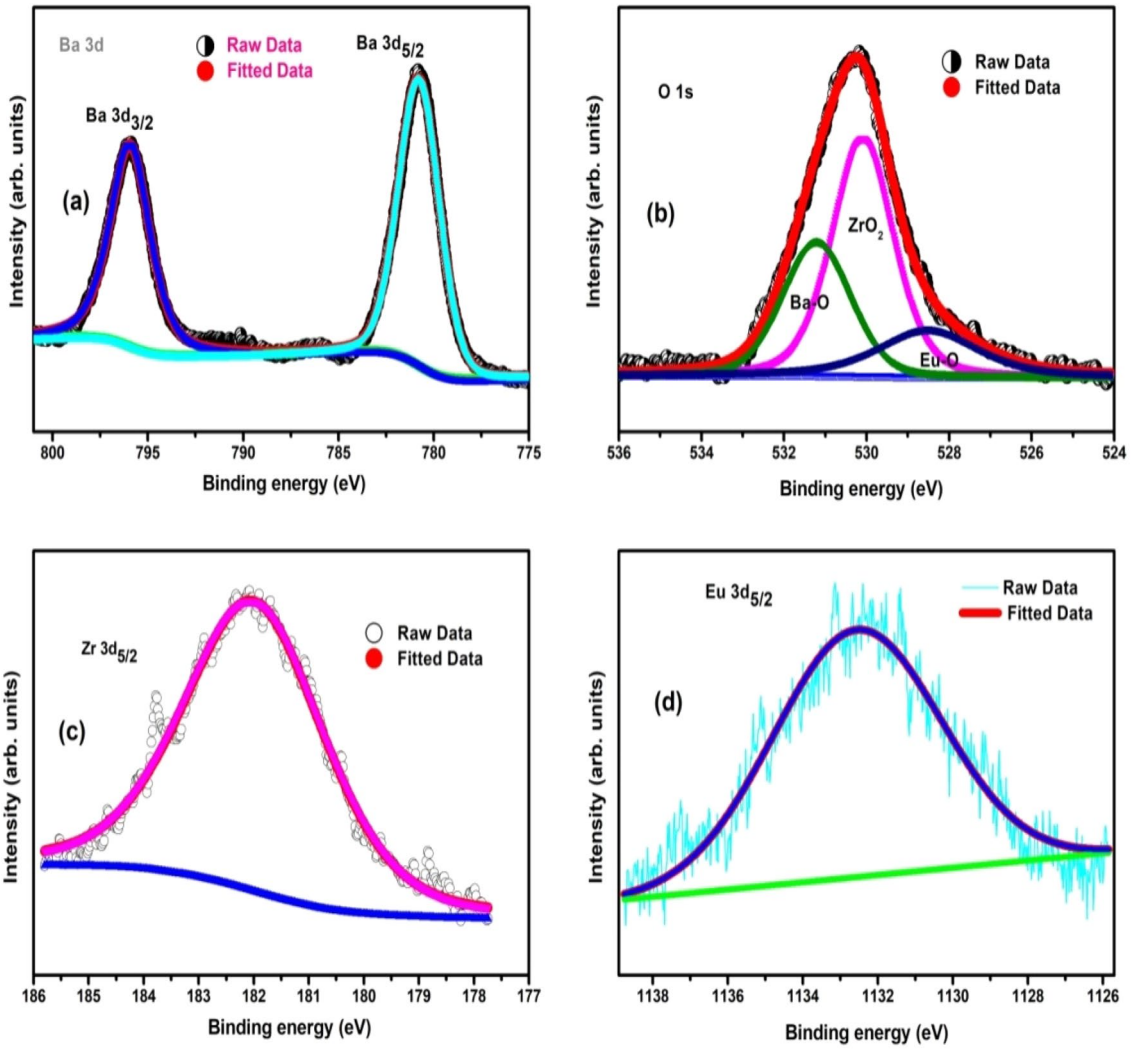

Fig. 4 **a** XPS Ba*3d* core level spectrum of $Ba_3Zr_2O_7$: Eu^{3+} in the range 800–775 eV **b** XPS O *1 s* core level spectrum of $Ba_3Zr_2O_7$: Eu^{3+} in the range 536–524 eV **c** XPS Zr *3d* core level spectrum of $Ba_3Zr_2O_7$: Eu^{3+} in the range 186–177 eV **d** XPS Eu *3d* core level spectrum of $Ba_3Zr_2O_7$: Eu^{3+} in the range 1138–1126 eV

profile which indicates that the samples synthesized by the combustion route have been well crystallized [26].

5.2 Concentration quenching

The emission spectra of $Ba_3Zr_2O_7$: Eu^{3+} at a different molar concentration of Eu^{3+} (0.5, 1, 1.5, 2, 2.5, 3, 3.5, and 4 mol.%) ion are shown in Fig. 7. The spectra are monitored at an excitation wavelength of 392 *nm* in the region 500–750 nm. It is observed that the peak profile of all the different concentrations of Eu^{3+} ions is same but the phosphorescence intensities are changing with the increase in the concentration of Eu^{3+} ion in the host lattice. This variation in the PL intensity with the increase in Eu^{3+} ion concentration is shown in the inset of Fig. 7. The maximum emission intensity of the prominent peak (613 nm) is observed at 2 mol.% afterward, the emission intensity starts declining with the increase in the concentration of Eu^{3+} ion due to the concentration quenching effect [38]. In this phenomenon, the cross-relaxation process occurs with the increase in the Eu^{3+}concentration when the distance between Eu^{3+}–Eu^{3+} ions is less than the critical value and the non-radiative transition takes place when the excitation energy is lost to the killer sites.

To know the exact reason for the concentration quenching phenomenon, Dexter [39] has given an Eq. (5) to find the interaction between the activator (Eu^{3+}-Eu^{3+}) ions in the host lattice.

$$\frac{I}{x} = K[1 + \beta(x)^{Q/3}]^{-1} \tag{5}$$

where I is the intensity, K and β are constants, x is the value of activator (Eu^{3+}) ion concentration greater than

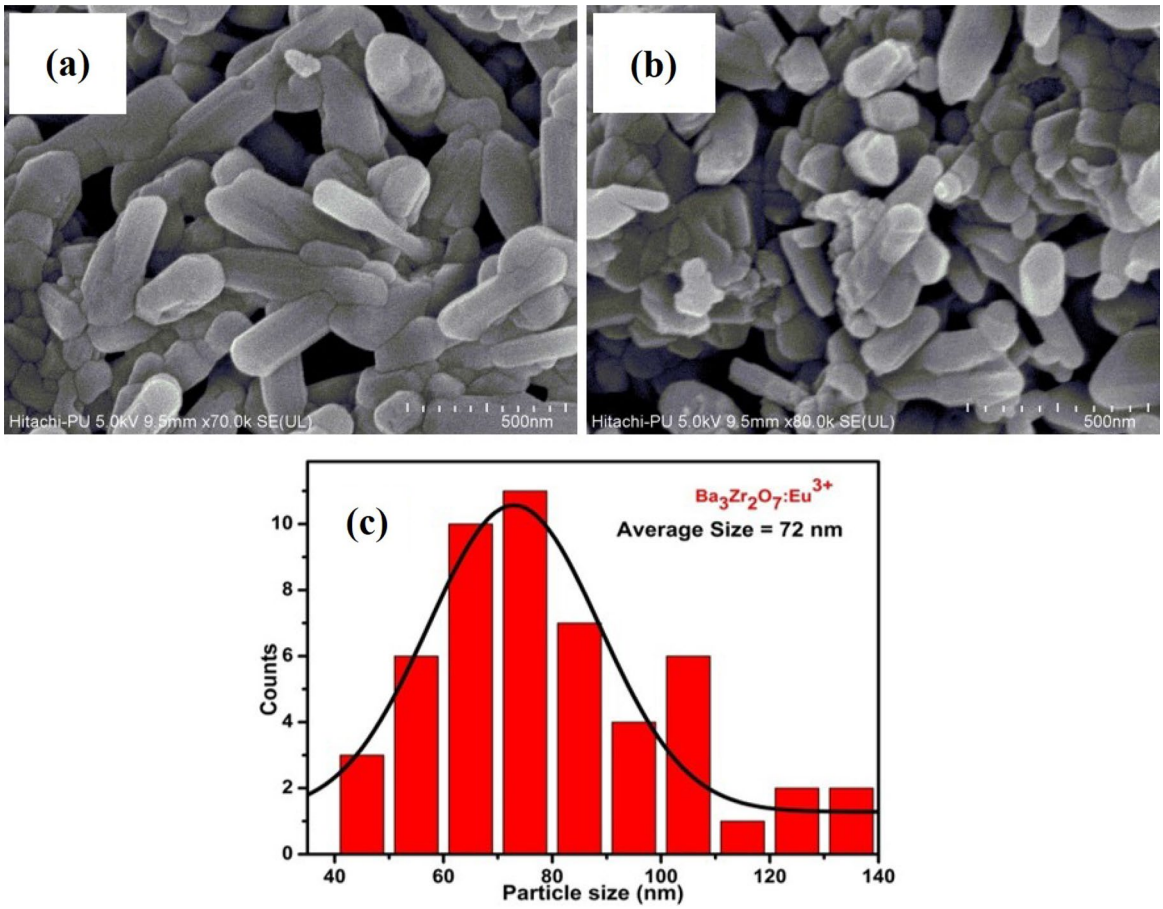

Fig. 5 **a** and **b** FESEM image of $Ba_3Zr_2O_7$: Eu^{3+} (2 mol.%) phosphor and **c** Particle size distribution histogram of $Ba_3Zr_2O_7$: Eu^{3+} (2 mol.%)

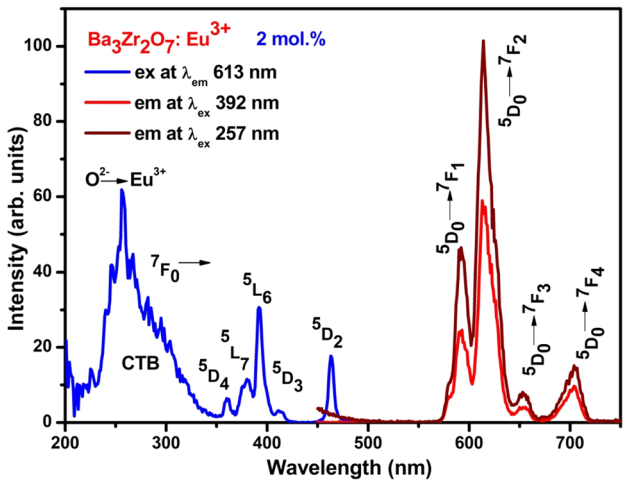

Fig. 6 PL excitation and emission of $Ba_3Zr_2O_7$: Eu^{3+} (2 mol.%) in the range 200–750 nm

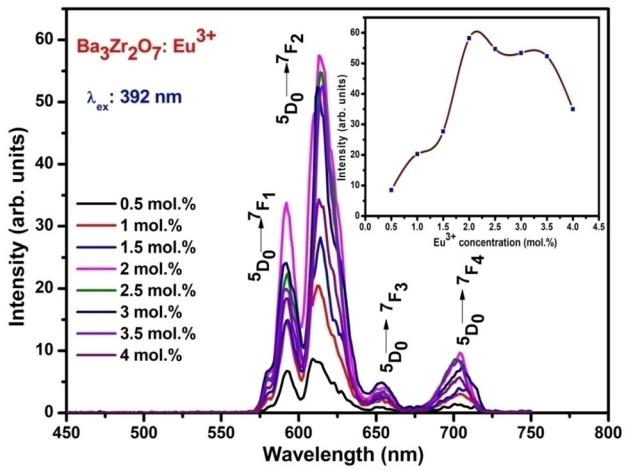

Fig. 7 PL emission spectra of $Ba_3Zr_2O_7$: Eu^{3+} at different Eu^{3+} concentration (0.5, 1, 1.5, 2, 2.5, 3, 3.5, and 4 mol.%) and inset shows the variation of PL intensity with Eu^{3+} concentration

the optimum molar concentration, and Q is the multipolar interaction. The value of Q illustrate the type of interaction, i.e., 3 (exchange interaction), 6 (dipole–dipole interaction), 8 (dipole-quadrupole), and 10 (quadrupole–quadrupole interaction). Figure 8 shows the plot between Log(X) on the

x-axis and Log (I/X) on the y-axis of $Ba_3Zr_2O_7$: Eu^{3+} phosphor at emission intensity of wavelength 613 nm. The graph is fitted by a straight line that has a slope of -1.82919, and the obtained value of Q is 5.5 which is close to 6. This value of Q reveals that the dipole–dipole interaction is responsible for the concentration quenching phenomenon in the $Ba_3Zr_2O_7$: Eu^{3+} phosphor.

5.3 Photometric studies

The colorimetric performance is important to know that the synthesized material is a good phosphor. So, in the photometric study, the Commission International de I'Eclairage (CIE) coordinates and Correlated Color Temperature (CCT) are evaluated. The chromaticity coordinates of $Ba_3Zr_2O_7$: Eu^{3+} (0.5–4 mol.%) phosphor are calculated based on the PL spectra and are shown in Fig. 9. The CIE calculated software [40] is used to obtain the chromaticity coordinates of the synthesized phosphor. Alexander et al. [41] have reported the structural and spectroscopic investigations of europium oxalate nanocrystals, and the obtained CIE coordinates of the crystals are (0.66, 0.31) at 394 nm excitation. Ramteke et al. [42] have studied the photoluminescence properties of Eu^{3+}-activated $Ba_2Mg(PO_4)_2$ phosphor, and they have observed that the CIE coordinates of the phosphor at wavelength 592 nm are (0.586, 0.412) and for wavelength 615 nm are (0.680, 0.319) under 396 nm excitation. Gupta et al. [43] have studied the photoluminescence properties of $Nd_2Zr_2O_7$: Eu^{3+} phosphor, and the obtained CIE coordinates are (0.614, 0.312) which gives intense red emission. In this work, the obtained CIE coordinates of $Ba_3Zr_2O_7$: Eu^{3+}(0.5–4 mol.%) phosphor are shown in Table 2 and the values are in close agreement with the reported values. These calculated values fall in the red color region of the color gamut. Therefore, it is a good red emitter.

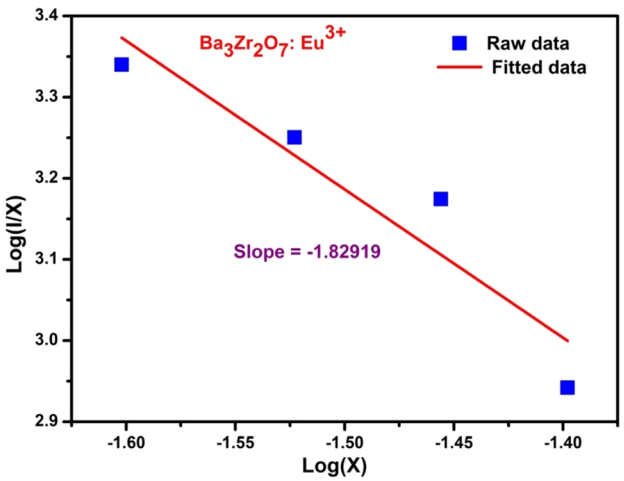

Fig. 8 A plot between Log(X) and Log (I/X) of $Ba_3Zr_2O_7$: Eu^{3+} phosphor at emission intensity of wavelength 613 nm

The CCT is calculated using McCamy empirical formula [44] given in Eq. (6).

$$CCT = -437n^3 + 3601n^2 - 6861n + 5514.32 \tag{6}$$

$$n = \frac{(x - x_e)}{(y - y_e)}$$

where n is the inverse of slope line, x_e and y_e are the chromaticity epicenter, and x and y are CIE coordinates of the sample. The value of chromaticity epicenter is $x_e = 0.3320$, and $y_e = 0.1858$. In the present study, the CCT values of $Ba_3Zr_2O_7$: Eu^{3+}(0.5–4 mol.%) are shown in Table 2 and found that the values are less than 5000 K. Usually, if the CCT value is less than 5000 K then it is warm white light used in home appliances and if the CCT value is greater than 5000 K then it is cold white light which is used for commercial lighting purpose.

This PL result reveals that the synthesized material has potential application as a promising red phosphor under near UV excitation for white light-emitting diodes (WLEDs). It can be used as warm white light in bedrooms, living rooms, hallways, etc.

6 Optical studies

6.1 Diffuse reflectance study

The diffuse reflectance spectra (DRS) of the synthesized series of Eu^{3+} (0–4 mol.%)-activated $Ba_3Zr_2O_7$ phosphor are shown in Fig. 10. $BaSO_4$ is used as a standard reference throughout measuring the data for all the samples, and the spectra are recorded in the region 190–1400 nm. In the UV region of wavelength range 190–290 nm, a sharp band is obtained due to the charge transfer band from ligands (O^{2-}) to the rare-earth (Eu^{3+}) in the host lattice. At 254 nm the intense band is observed which shows that at this region the light is absorbed and corresponds to the bandgap of the material [45]. In the wavelength region 430–480 nm feebly absorption band is observed because of the *4f–4f* transition of Eu^{3+} ion. The DRS is a standard method to obtain the bandgap of the powder samples.

6.2 Bandgap determination

The bandgap of the synthesized materials is obtained from diffuse reflectance spectra (DRS) using the Kubelka–Munk theory [46] given in Eq. (7)

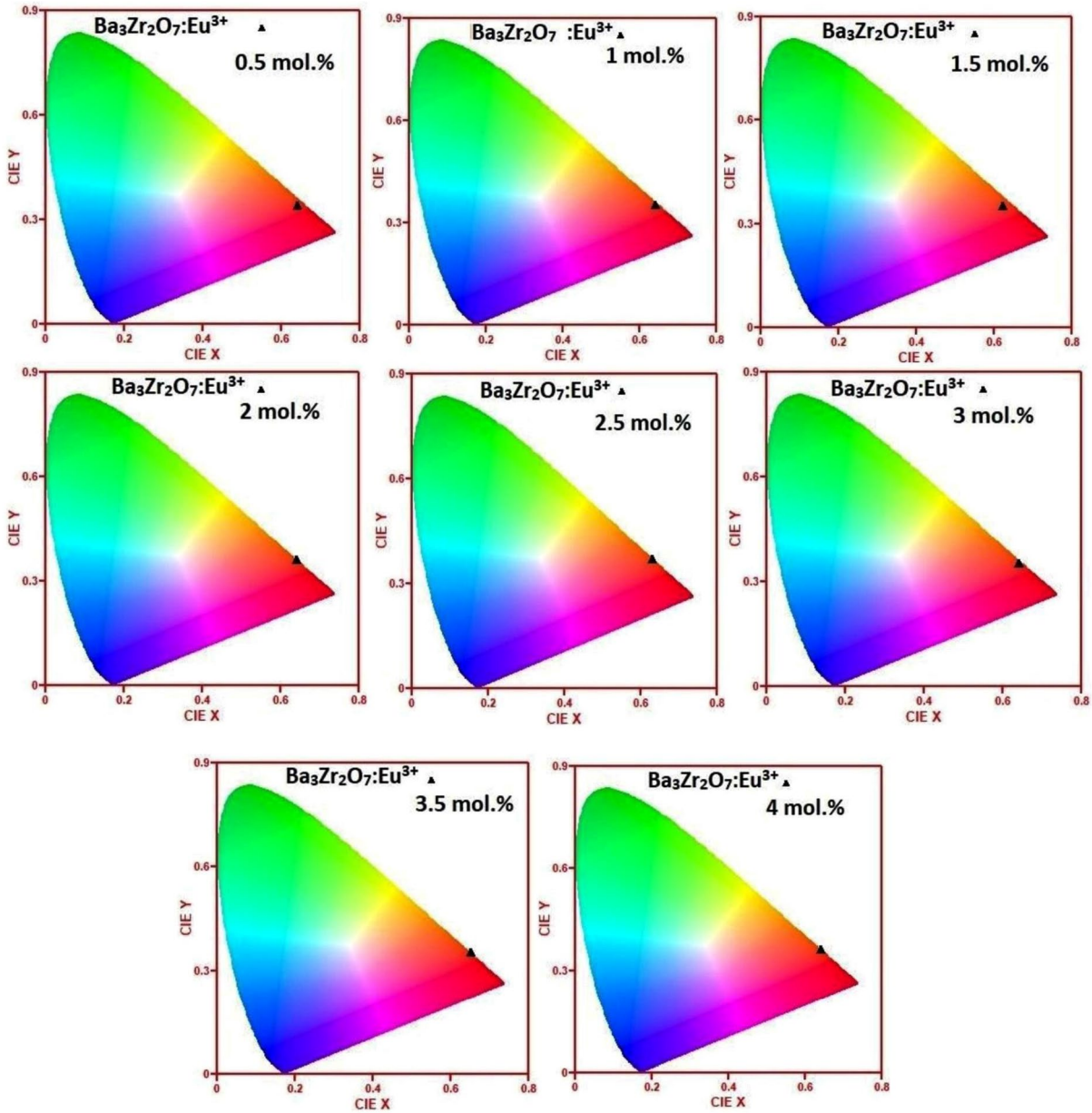

Fig. 9 CIE coordinates of $Ba_3Zr_2O_7$: Eu^{3+} (0.5, 1, 1.5, 2, 2.5, 3, 3.5, 4 mol.%)

$$F(R) = \frac{(1-R)^2}{2R} = \frac{K}{S} \tag{7}$$

where R is the diffuse reflectance, K is the molar absorption coefficient, and S is the scattering coefficient. This theory converts the diffused reflectance spectrum into the absorbance spectrum and using Tauc relation [47] an optical bandgap of the material can be obtained.

$$(\alpha h\nu)^2 = A\left(h\nu - E_g\right) \tag{8}$$

where α is a linear absorption coefficient of a material, $h\nu = (1239.7/\lambda(nm))$ is the energy of a photon in eV, E_g is the bandgap of material, and A is the constant of proportionality. By replacing α by F(R) in the above equation, we get a modified equation as:

$$[F(R)h\nu]^2 = A\left(h\nu - E_g\right) \tag{9}$$

As a result, the bandgap of the material is obtained by extrapolating the linear fitted region on the horizontal axis, i.e., the x-axis $\left([F(R)h\nu]^2 = 0\right)$.

Table 2 CIE coordinates and CCT values of $Ba_3Zr_2O_7$: Eu^{3+} (0.5–4 mol.%)

Concentration of Eu^{3+} ion (mol.%)	CIE x, y	CCT (K)
0.5	0.64, 0.34	2695.27
1	0.64, 0.35	2434.50
1.5	0.62, 0.35	2206.04
2	0.64, 0.36	2222.33
2.5	0.63, 0.37	1988.87
3	0.64, 0.35	2434.50
3.5	0.65, 0.35	2523.66
4	0.64, 0.36	2222.33

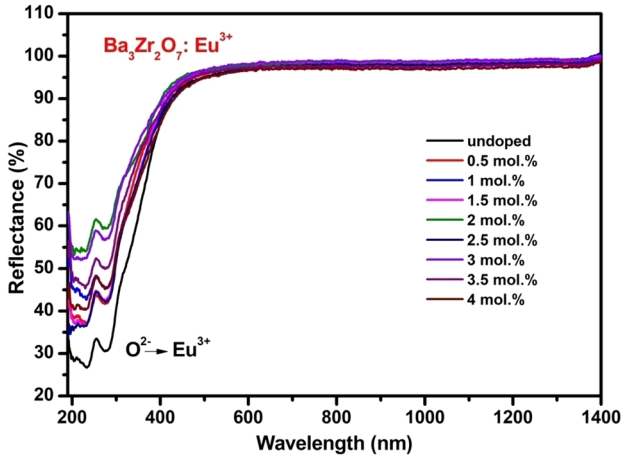

Fig. 10 Diffuse reflectance of $Ba_3Zr_2O_7$: Eu^{3+} (0–4 mol.%) in the range 190–1400 nm

The bandgap of the synthesized series Eu^{3+} (0–4 mol.%)-activated $Ba_3Zr_2O_7$ phosphor is shown in Fig. 11. In this study, the obtained value of bandgap for all the molar concentrations is in the range of 4.62–4.83 eV. It is observed that with the increase in the molar concentration of Eu^{3+} ion in the host lattice, the bandgap of the material increases up to 2 mol.% because of the Burstein-Moss effect [48]. Thereafter, the bandgap decreases with the increase in the concentration of Eu^{3+} ion in the host lattice due to the band narrowing effect [49]. This is may be due to the formation of sub-levels between the conduction and valence band. Also, a hump-like feature is observed in the energy range 3.5–4.5 eV. The feature may be appeared due to the presence of a secondary phase in the host and doped samples which is also confirmed from the XRD result, i.e., the minimal intensity peak has been observed in the XRD pattern.

6.3 Refractive index and metallization criterion

Refractive index and metallization criterion are also important parameters to study the optical property of the material. The variation in the bandgap, refractive index, and metallization criterion is shown in Fig. 12. The relation between the refractive index and optical bandgap [50] is given by Eq. (10)

$$\frac{n^2-1}{n^2+2} = 1 - \frac{(E_g)^{1/2}}{(20)^{1/2}} \tag{10}$$

where n is the refractive index of the material, and E_g is the bandgap of the material.

Metallization criterion is given by Dimitrov and Sakka [51]. It is used to study the nature of the material, i.e., metallic or insulating. The calculation of this parameter is based on the refractive index and the bandgap of the material which is given by Eq. (11)

$$M = 1 - \frac{n^2-1}{n^2+2} = \frac{(E_g)^{1/2}}{(20)^{1/2}} \tag{11}$$

where M is the metallization criterion. Generally, when the value of M is less than 1 ($M<1$), then the material is non-metallic, and when the value of M is greater than 1 ($M>1$), then the material is metallic. In this study, for all the samples the value of M is less than 1 which indicates the non-metallic nature of the samples. The variation in values of bandgap, refractive index, and metallization criterion for all the synthesized samples are listed in Table 3.

7 Conclusion

The present study shows that $Ba_3Zr_2O_7$: Eu^{3+} phosphors are successfully synthesized via the solution combustion method. XRD result confirmed the tetragonal crystal system with space group 14/mmm (139), and the lattice parameters found to be $a=4.35$ (Å) and $c=21.7$ (Å) are well-matched with the standard JCPDS card. XPS results affirmed the presence of Ba, Zr, O, and Eu having a charge state of 2+, 4+, 2-, and 3+, respectively. FESEM result shows the mixed morphology comprised of some spheres and plates. The four PL emission bands are obtained at 591 nm ($^5D_0 \rightarrow {}^7F_1$), 613 nm ($^5D_0 \rightarrow {}^7F_2$), 655 nm ($^5D_0 \rightarrow {}^7F_3$), and 704 nm ($^5D_0 \rightarrow {}^7F_4$) under 392 nm excitation. The CIE chromaticity coordinates of optimum molar concentration (2 mol.%) are found to be (0.64, 0.36) which exhibit intense red emission and the phosphor may be used for white light-emitting diodes (WLEDs) under near UV excitation. The values of optical bandgap, refractive index, and metallization

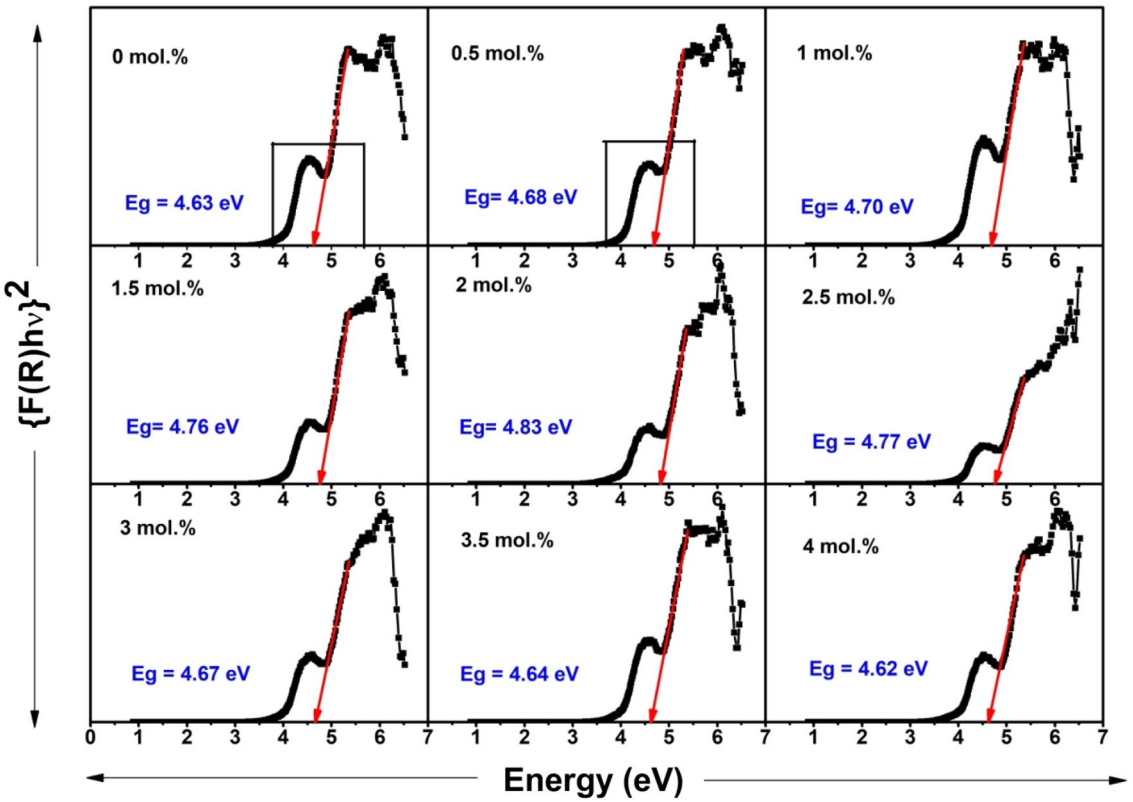

Fig. 11 Energy band gap of $Ba_3Zr_2O_7$: Eu^{3+} (0–4 mol.%)

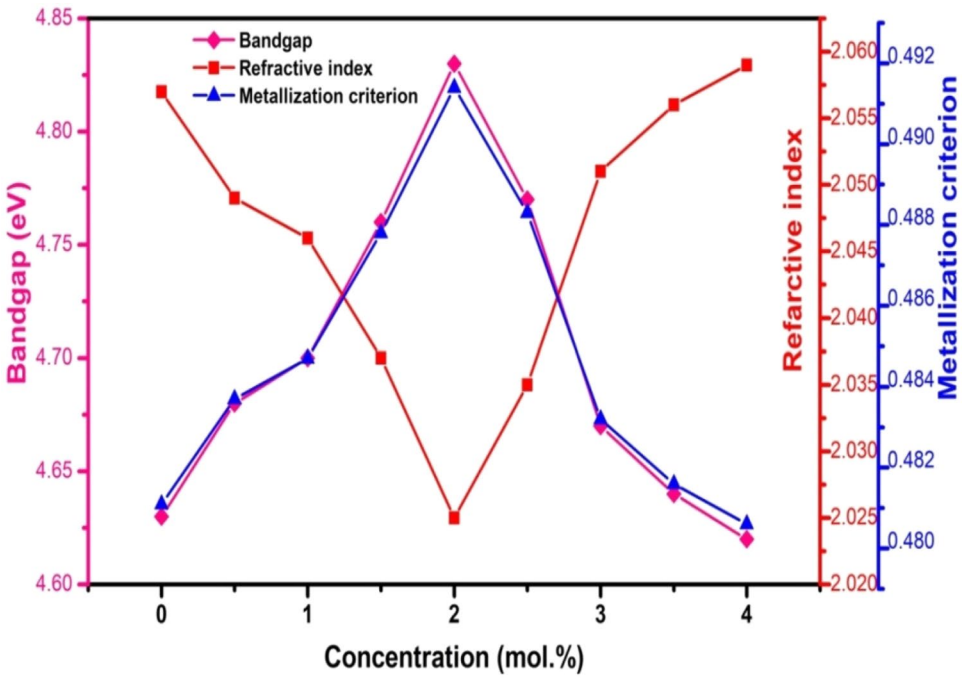

Fig. 12 Variation in the bandgap. refractive index, and metallization criterion with Eu^{3+} ion concentration (0–4 mol.%) in $Ba_3Zr_2O_7$ phosphor

Table 3 Variation in the bandgap, refractive index, and metallization criterion of Eu^{3+}-activated $Ba_3Zr_2O_7$ phosphor

Concentration of Eu^{3+} ion (mol.%)	Bandgap E_g(eV)	Refractive index N	Metallization criterion M
0	4.63	2.057	0.4811
0.5	4.68	2.049	0.4837
1	4.70	2.046	0.4847
1.5	4.76	2.037	0.4878
2	4.83	2.025	0.4914
2.5	4.77	2.035	0.4883
3	4.67	2.051	0.4832
3.5	4.64	2.056	0.4816
4	4.62	2.059	0.4806

criterion of $Ba_3Zr_2O_7$: Eu^{3+} (0–4 mol.%) are obtained in the range of 4.62–4.83 eV, 2.025–2.059, and 0.4806–0.4914, respectively.

Acknowledgements The authors humbly acknowledge Dr. Mukul Gupta, Scientist, UGC-DAE CSR, Indore for providing the XRD facility. We are also grateful to Mr. AvinashWadikar and Mr. Sharad Karwal for helping in XPS measurements at the Indus-1 synchrotron radiation source.

References

1. R. Yan, Y. Li, Down/Up conversion in Ln^{3+}-doped YF_3 nanocrystals. Adv. Funct. Mater. **15**, 763–770 (2005)
2. L.X. Lovisa, V.D. Araújo, R.L. Tranquilin, E. Longo, M.S. Li, C.A. Paskocimas, M.R.D. Bomio, F.V. Motta, White photoluminescence emission from ZrO_2 co-doped with Eu^{3+}, Tb^{3+} and Tm^{3+}. J. Alloys Compd. **674**, 245–251 (2016)
3. Y.C. Yan, A.J. Faber, H. de Waa, P.G. Kik, A. Polman, Erbium-doped phosphate glass waveguide on silicon with 4.1 dB/cm gain at 1.535 mm. Appl. Phys. Lett. **71**, 2922–2924 (1997)
4. K. Omri, O.M. Lemine, L. El Mir, Mn doped zinc silicate nanophosphors with bifunctionality of green-yellow emission and magnetic properties. Ceram. Int. **43**, 6585–6591 (2017)
5. K.N. Shinde, S.J. Dhoble, A. Kumar, Combustion synthesis of Ce^{3+}, Eu^{3+} and Dy^{3+} activated $NaCaPO_4$ phosphors. J. Rare Earth **29**, 527–535 (2011)
6. K. Omri, A. Alyamani, L. El Mir, Photoluminescence and cathodoluminescence of Mn doped zinc silicate nanophosphors for green and yellow field emissions displays. Appl. Phys. A **124**, 215–222 (2018)
7. K. Arik, P. Amitava, Recent advances on the optical properties of Eu^{3+} ion in nanosystems. J. Nanosci. Nanotechnol. **18**, 8047–8069 (2018)
8. T. Murata, T. Tanoue, M. Iwasaki, K. Morinaga, T. Hase, Fluorescence properties of Mn^{4+} in $CaAl_{12}O_{19}$ compounds as red-emitting phosphor for white LED. J. Lumin. **114**, 207–212 (2005)
9. J. Cho, J.H. Park, J.K. Kim, E.F. Schubert, White light-emitting diodes: history, progress, and future. Laser Photon Rev. **11**, 1600147–1600157 (2017)
10. D.K. Yim, I.S. Cho, C.W. Lee, J.H. Noh, H.S. Roh, K.S. Hond, Preparation and photoluminescence properties of γ-$KCaPO_4$:Eu^{2+} for near UV-based white LEDs. Opt. Mater. **33**, 1036–1040 (2011)
11. I. Omkaram, G.S.R. Raju, S. Buddhudu, Emission analysis of Tb^{3+}:$MgAl_2O_4$ powder phosphor. J. Phys. Chem. Solids **69**, 2066–2069 (2008)
12. A.K. Kunti, N. Patra, R.A. Harris, S.K. Sharma, D. Bhattacharyya, S.N. Jha, H.C. Swart, Local structure and spectroscopic properties of Eu^{3+}-doped $BaZrO_3$. Inorg. Chem. **58**, 3073–3089 (2019)
13. I. Omkaram, S. Buddhudu, Photoluminescence properties of $MgAl_2O_4$:Dy^{3+} powder phosphor. Opt. Mater. **32**, 8–11 (2009)
14. V. Singh, T.K.G. Rao, D.K. Kim, Characterization, photoluminescence and correlation between thermoluminescence and ESR of combustion synthesized $CaAl_2O_4$: Sm^{3+}material. Radiat. Meas. **43**, 1198–1203 (2008)
15. P. Li, Z. Yang, Z. Wang, Q. Guo, White light emitting diodes of UV-based$Sr_3Y_2(BO_3)_4$:Dy^{3+} and luminescent properties. Mater. Lett. **62**, 1455–1457 (2008)
16. P. Gupta, A.K. Bedyal, V. Kumar, Y. Khajuria, S.P. Lochab, S.S. Pitale, O.M. Ntwaeaborwa, H.C. Swart, Photoluminescence and thermoluminescence properties of Tb^{3+} doped $K_3Gd(PO_4)_2$ nanophosphor. Mater. Res. Bull. **60**, 401–411 (2014)
17. T. Nakajima, M. Isobe, T. Tsuchiya, Y. Ueda, T. Manabe, Photoluminescence property of vanadates $M_2V_2O_7$ (M: Ba, Sr and Ca). Opt. Mater. **32**, 1618–1621 (2010)
18. P. Khajuria, R. Mahajan, S. Kumar, R. Prakash, R.J. Choudhary, D.M. Phase, Surface and spectral investigation of Sm^{3+} doped MgO-ZrO_2 phosphors. Optik **216**, 164909–164919 (2020)
19. V. Singh, S. Watanabe, T.K. GunduRao, K. Al-Shamery, M. Haase, Y.D. Jho, Synthesis, characterisation, luminescence and defect centres in solution combustion synthesized $CaZrO_3$:Tb^{3+} phosphor. J. Lumin. **132**, 2036–2042 (2012)
20. S. Stolen, E. Bakken, C.E. Mohn, Oxygen-deficient perovskites: linking structure, energetics and ion transport. Phys. Chem. Chem. Phys. **8**, 429–447 (2006)
21. S.H. Butt, M.S. Rafique, K. Siraj, A. Latif, A. Afzal, M.S. Awan, S. Bashir, N. Iqbal, Epitaxial thin-film growth of ruddlesden–popper-type $Ba_3Zr_2O_7$ from a $BaZrO_3$ target by pulsed laser deposition. Appl. Phys. A **122**, 658–666 (2016)
22. Sheetal, V. B. Taxak, S. Singh, Mandeep, S. P. Khatkar, Synthesis and optical properties of red emitting Eu doped $CaZrO_3$ phosphor. Optik 125, 6340-6343 (2014)
23. R. Ramesh, N.A. Spaldin, Multiferroics: progress and prospects in thin films. Nat. Mater. **6**, 21–29 (2007)
24. C.C. Homes, T. Vogt, S.M. Shapiro, S. Wakimoto, A.P. Ramirez, Optical response of high-dielectric-constant perovskite-related oxide. Science **293**, 673–676 (2001)
25. S.K. Gupta, P.S. Ghosh, N. Pathak, A. Arya, V. Natarajan, Understanding the local environment of Sm^{3+} in doped $SrZrO_3$ and energy transfer mechanism using time-resolved luminescence: a combined theoretical and experimental approach. RSC Adv. **4**, 29202–29215 (2014)
26. S.N. Ruddlesden, P. Popper, The compound $Sr_3Ti_2O_7$ and its structure. Acta Cryst. **11**, 54–55 (1958)
27. S.K. Gupta, N. Pathak, R.M. Kadam, An efficient gel-combustion synthesis of visible light emitting barium zirconate perovskite nanoceramics: probingthephotoluminescence of Sm^{3+} and Eu^{3+} doped $BaZrO_3$. J. Lumin. **169**, 106–114 (2016)
28. B. Marı´, K.C. Singh, M. Sahal, S.P. Khatkar, V.B. Taxak, M. Kumar, Preparation and luminescence properties of Tb^{3+} doped ZrO_2 and $BaZrO_3$ phosphors. J. Lumin. **130**, 2128–2132 (2010)
29. K.C. Patil, S.T. Aruna, S. Ekambaram, Combustion synthesis. Curr. Opin. Solid State Mater. Sci. **2**, 158–165 (1997)
30. Q. Du, G. Zhou, S. Zhang, X. Jia, H. Zhou, Z. Yang, Facile combustion synthesis of novel $CaZrO_3$:Eu^{3+}, Gd^{3+} red phosphor and remarkably enhanced photoluminescence by Gd^{3+} doping. Bull. Mater. Sci. **38**, 215–220 (2015)
31. B.D. Cullity, *Element of X-Ray Diffraction* (Addison-Wesley, New York, 1956), pp. 107–113

32. L.L. Jiang, X.G. Tang, S.J. Kuang, H.F. Xiong, Surface chemical states of barium zirconate titanate thin films prepared by chemical solution deposition. Appl. Surf. Sci. **255**, 8913–8916 (2009)
33. F. Mercier, C. Alliot, L. Bion, N. Thromat, P. Toulhoat, XPS study of Eu(III) coordination compounds: Core levels binding energies in solid mixed-oxo-compounds $Eu_mX_xO_y$. J. Electron Spectrosc. Relat. Phenom. **150**, 21–26 (2006)
34. N. Mahanta, J.P. Chen, A novel route to the engineering of zirconium immobilized nano-scale carbon for arsenate removal from water. J. Mater. Chem. A **1**, 8636–8644 (2013)
35. D. Kim, Y.H. Jin, K.W. Jeon, S. Kim, S.J. Kim, O.H. Han, D.K. Seo, J.C. Park, Blue-silica by Eu^{2+}-activator occupied in interstitial sites. RSC Adv. **5**, 74790–74801 (2015)
36. M. Jiao, N. Guo, W. Lü, Y. Jia, W. Lv, Q. Zhao, B. Shao, H. You, Synthesis, structure and photoluminescence properties of europium-, terbium-, and thulium-doped $Ca_3Bi(PO_4)_3$ phosphors. Dalton Trans. **42**, 12395–12402 (2013)
37. W. Hami, D. Zambon, A. Zegzoutia, M. Elaatmani, M.E. Ghozzi, M. Daou, Application of spectroscopic properties of Eu^{3+} ion to predict the site symmetry of active ions in $AgLaP_2O_7$: Eu^{3+} phosphors. Inorg. Chem. Commun. **107**, 107475–107483 (2019)
38. G. Blasse, B. C. Grabmaier, Luminescent Materials, (Springer-Verlag, Berlin Heidelberg, 1994) ISBN 978-3-642-79017-1
39. D.L. Dexter, A theory of sensitized luminescence in solids. J. Chem. Phys. **21**, 836–851 (1953)
40. http://WWW.mathworks.com.matlabcentral/fileexchange/29620 ciecoordinate- calculator (last accessed on 09/04/2021)
41. D. Alexander, K. Thomas, M. Joy, P.R. Biju, N.V. Unnikrishnan, C. Joseph, Structural and spectroscopic investigations on the quenching free luminescence of europium oxalate nanocrystals. Acta Cryst. **75**, 589–597 (2019)
42. S.K. Ramteke, N.S. Kokode, A.N. Yerpude, G.N. Nikhare, S.J. Dhoble, Synthesis and photoluminescence properties of Eu^{3+}-activated $Ba_2Mg(PO_4)_2$ phosphor. Lumin **35**, 618–621 (2020)
43. S.K. Gupta, C. Reghukumar, R.M. Kadam, Eu^{3+} local site analysis and emission characteristics of novel $Nd_2Zr_2O_7$: Eu phosphor: insight into the effect of europium concentration on its photoluminescence properties. RSC Adv. **6**, 53614–53624 (2016)
44. C.S. McCamy, Correlated color temperature as an explicit function of chromaticity coordinates. Color Res. Appl. **17**, 142–144 (1992)
45. S. Som, A. Choubey, S.K. Sharma, Spectral and trapping parameters of Eu^{3+} in Gd_2O_2S nanophosphors. J. Exp. Nanosci. **10**, 350–370 (2013)
46. A.E. Morales, E.S. Mora, U. Pa, Use of diffuse reflectance spectroscopy for optical characterization of unsupported nanostructures. Rev. Mex. Fis. S **53**, 18–22 (2007)
47. J. Tauc, A. Menth, States in the gap. J. Non-Cryst. Solids **8**, 569–585 (1972)
48. M. Grundmann, The physics of semiconductors, (Springer Berlin Heidelberg, New York, 2006) ISBN 978-3-642-13884-3
49. A.S. Ahmed, S.M. Muhamed, M.L. Singla, S. Tabassum, A.H. Naqvi, A. Azam, Band gap narrowing and fluorescence properties of nickel doped SnO_2 nanoparticles. J. Lumin. **131**, 1–6 (2011)
50. B. Samanta, D. Dutta, S. Ghosh, Synthesis and different Optical properties of Gd_2O_3 doped sodium zinc tellurite glasses. Phys. B: Phys. Condens. Matter. **515**, 82–88 (2017)
51. V. Dimitrov, S. Sakka, Linear and nonlinear optical properties of simple oxides. II. J. Appl. Phys. **79**, 1741–1745 (1996)